SCIENTIFIC REPORTS

OPEN

SUBJECT AREAS:
OPTICAL IMAGING
SPECTROSCOPY
LASER-PRODUCED PLASMAS

Received
7 May 2014

Accepted
25 July 2014

Published
14 August 2014

Correspondence and requests for materials should be addressed to V.M.-R. (vincent.motto-ros@univ-lyon1.fr)

* These authors contributed equally to this work.

Laser spectrometry for multi-elemental imaging of biological tissues

L. Sancey*, V. Motto-Ros*, B. Busser, S. Kotb, J. M. Benoit, A. Piednoir, F. Lux, O. Tillement, G. Panczer & J. Yu

Institut Lumière Matière, UMR5306 Université Lyon 1-CNRS, Université de Lyon 69622 Villeurbanne cedex, France.

An increasing interest has arisen in research focused on metallic and organic ions that play crucial roles in both physiological and pathological metabolic processes. Current methods for the observation of trace elements in biological tissues at microscopic spatial resolution often require equipment with high complexity. We demonstrate a novel approach with an all-optical design and multi-elemental scanning imaging, which is unique among methods of elemental detection because of its full compatibility with standard optical microscopy. This approach is based on laser-induced breakdown spectroscopy (LIBS), which allows the elements in a tissue sample to be directly detected and quantified under atmospheric pressure. We successfully applied this method to murine kidneys with 10 µm resolution and a ppm-level detection limit to analyze the renal clearance of nanoparticles. These results offer new insight into the use of laser spectrometry in biomedical applications in the field of label-free elemental mapping of biological tissues.

Optical microscopy has served as a remarkably effective tool for medical and biological research for more than three centuries, and advanced technologies are pushing back the technical limitations inherent to optical imaging microscopy. Among these advanced technologies, the most significant are those that extend the spatial resolution[1–4] or improve access for deeper *in vivo* imaging[5–8] and label-free microscopy techniques based on Raman scattering for molecular imaging[9–12]. However, the elemental imaging of biological materials still requires equipment of a high level of complexity and vacuum operation conditions, such as synchrotron radiation microanalysis (SXRF)[13–16], nano secondary ion mass spectrometry (nano-SIMS)[17] or laser ablation inductively coupled plasma mass spectrometry (LA-ICP-MS)[18–21]. Although these approaches offer high performance, the complexity of the required equipment renders the analysis very restrictive and leads to difficulty in applying these methods in research laboratories for routine elementary investigations. This limitation constitutes a major hindrance to the development of emerging biological research regarding endogenous and exogenous metals and metalloproteins, which play central roles in cell metabolism and, by extension, in every form of life. The dysregulation of these substances often leads to disease, and there is an increasing interest in analyzing elemental distributions in biological specimens to gain a better understanding of physiological and pathological processes[21,22].

In this study, we developed a laser spectrometry method that is compatible with standard microscopy systems for imaging and quantifying elemental distributions in biological organs with ppm-scale sensitivity and a pixel size of up to 10 × 10 µm^2. This approach uses the concept of a laser-induced plasma to elicit specific optical responses from inorganic elements that are either intrinsically contained in the biological tissue itself or artificially administered in the form of metals. This effective analytical technique, known as laser-induced breakdown spectroscopy (LIBS), is used for various applications[23,24], especially those that require field deployment, such as environmental monitoring[25], biochemical-agent detection[26] and space exploration[27,28]. The advantages of LIBS include its ease of use and speed of operation, as the material sampling, the atomization and the excitation steps occur simultaneously through single laser pulses. Elemental maps can then be obtained, in a pixel-by-pixel manner, by scanning the sample surface over the region of interest. Although LIBS scanning microanalysis has been reported for various types of solid materials[29–31], our group was the first to demonstrate its potential use for fresh biological tissues, although with a strict limit on the accessible resolution (100 µm) because of the complexity of mastering the laser ablation of such soft materials[32,33].

In this paper, we demonstrate a significant step toward multi-elemental LIBS imaging with unprecedented performance in terms of sensitivity and resolution for the analysis of biological tissues. These technological advancements required both a specific microscope configuration and a simple sample preparation (*i.e.*, epoxy

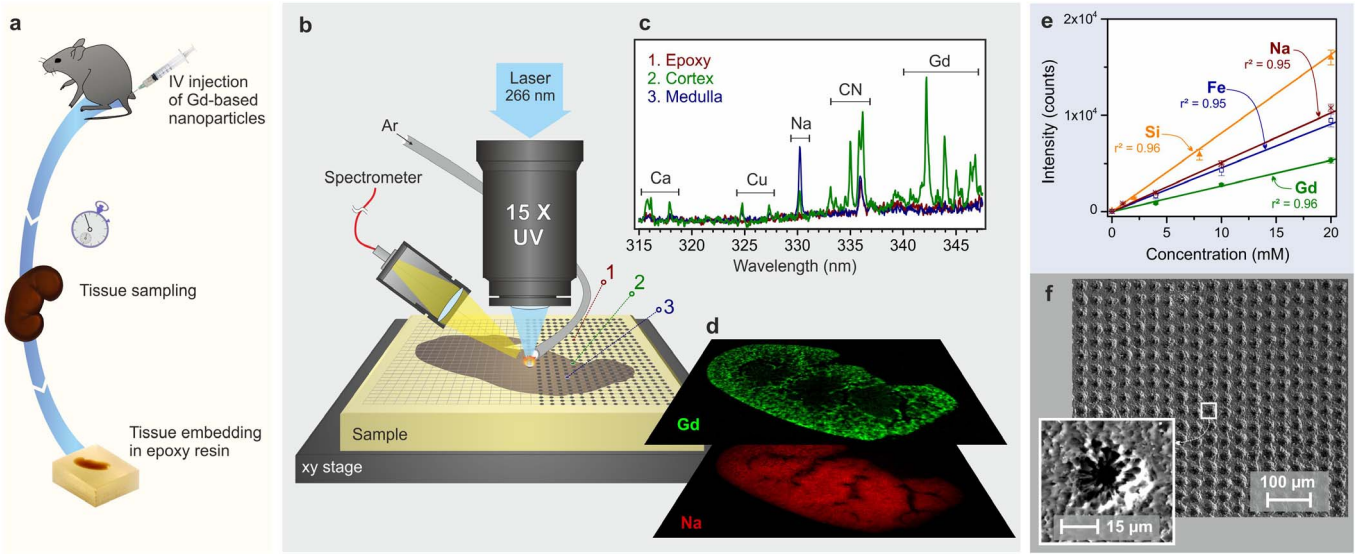

Figure 1 | General protocol for LIBS imaging. (a), Procedure for epoxy-embedded tissue sampling (drawing created by L. Sancey). (b), Schematic view of the LIBS experiment showing the major components, including the microscope objective, the motorized platform and the detection system. (c), Example of single-shot emission spectra recorded in the three different regions of the kidney indicated in (b) with characteristic emission lines of Gd, Na, Cu, and Ca. (d), Example of relative-abundance images for Gd and Na. (e), Calibration measurements illustrating the correlation between intensities and concentrations for the elements of interest. (f), Wide-angle and zoom images of the sample surface recorded via SEM after completion of the LIBS imaging scan.

embedding). The all-optical tabletop instrumentation we describe here allowed for a study of the renal clearance of theranostic gadolinium-based nanoparticles in rodents and aided in achieving a better understanding of the kinetics of a preclinical nanoparticle *in vivo*. These results offer new insight into the use of laser spectrometry in biomedical applications in the field of label-free elemental mapping of biological tissues.

Principle

The development of hybrid organic–inorganic nanoparticles has been a subject of strong interest in recent decades for applications such as drug delivery, DNA and protein recognition, and medical diagnosis and therapy[34–37]. Among the particles used for theranostic approaches (*i.e.,* for both diagnosis and therapy), ultra-small gadolinium-based nanoparticles known as AGuIX (with a size of less than 5 nm) were developed for multimodal imaging and radiotherapy guided by magnetic resonance imaging (MRI).38, 39 These particles are composed of a polysiloxane network surrounded by DOTA (1,4,7,10-tetraazacyclododecane-1,4,7,10-tetraacetic acid) derivatives covalently grafted to an inorganic matrix; DOTA is a chelating agent of gadolinium (Gd) and has already been used for clinical purposes (DOTAREM®, Guerbet, France). Because of their heterogeneous nature and potential applications, a characterization of the biological distribution of these nanoparticles in tissues and organs is a crucial step in preclinical evaluation. The biological evaluation of these nanoparticles is challenging because of their small size, which prevents the observation of individual particles using scanning electron microscopy. Moreover, labeling the nanoparticles with an organic fluorophore might affect their physicochemical properties in terms of their charge, size or shape, and thus their global and local distributions as well as their elimination with respect to both kinetics and the organs involved.

In this study, we focused on the renal clearance behavior of these ultra-small nanoparticles. The particles were intravenously administered to mice at the preclinical therapeutic dose, and the kidneys were sampled at various time points after injection. The organs were then embedded in epoxy and subsequently prepared before LIBS imaging using an ultramicrotome (Fig. 1a). Tissues are traditionally embedded in epoxy for electron microscopy; this step allows the tissue to be rapidly fixed without any alteration of its biological ultrastructure, and, moreover, it hardens the tissue and facilitates its sectioning[40,41]. In addition, calibration standards must also be prepared using the same epoxy resin.

In all LIBS experiments, nanosecond ultra-violet (266-nm) laser pulses with a 10-Hz repetition rate were focused by a 15× magnification objective to induce breakdown and sparking of the material (Fig. 1b). The light radiation emitted in the plasma was collected by a deported optical system and analyzed using a Czerny-Turner spectrometer equipped with an intensified charge-coupled device (ICCD) camera. The experiments were performed in ambient atmosphere with argon (Ar) gas flowing through the plasma region to improve the LIBS signal-to-noise ratio (SNR)[42]. The use of a computer-controlled xy stage enabled surface scanning along a predefined path such that an emission spectrum was recorded for each sampling position. These spectra collectively constituted a unique signature that was specific to each sample (Fig. 1c). After completion of the 2D raster, elemental images were created for each element of interest by selecting the specific emission lines and displaying their relative abundance in a false-color image, in which an arbitrary color was assigned for each element (Fig. 1d). The relative-abundance images were subsequently transformed into quantitative-abundance images after referring to calibration measurements performed on various standards (Fig. 1e).

In the present study, we focused our attention on 4 elements, 2 from the tissue itself (iron (Fe) and sodium (Na)) and 2 from the nanoparticles (Gd and silicon (Si)), although other elements, including phosphorus (P), magnesium (Mg), copper (Cu), and calcium (Ca), were also detected (Supplementary Fig. 1). In addition, two gold-standard observation techniques, scanning electron microscopy (SEM) and atomic force microscopy (AFM), were used to characterize the size and volume of the ablation craters (Fig. 1f).

Results

LIBS microanalysis performance. One challenging task in LIBS microanalysis is achieving an adequate balance between spatial resolution and detection sensitivity because the material sampling

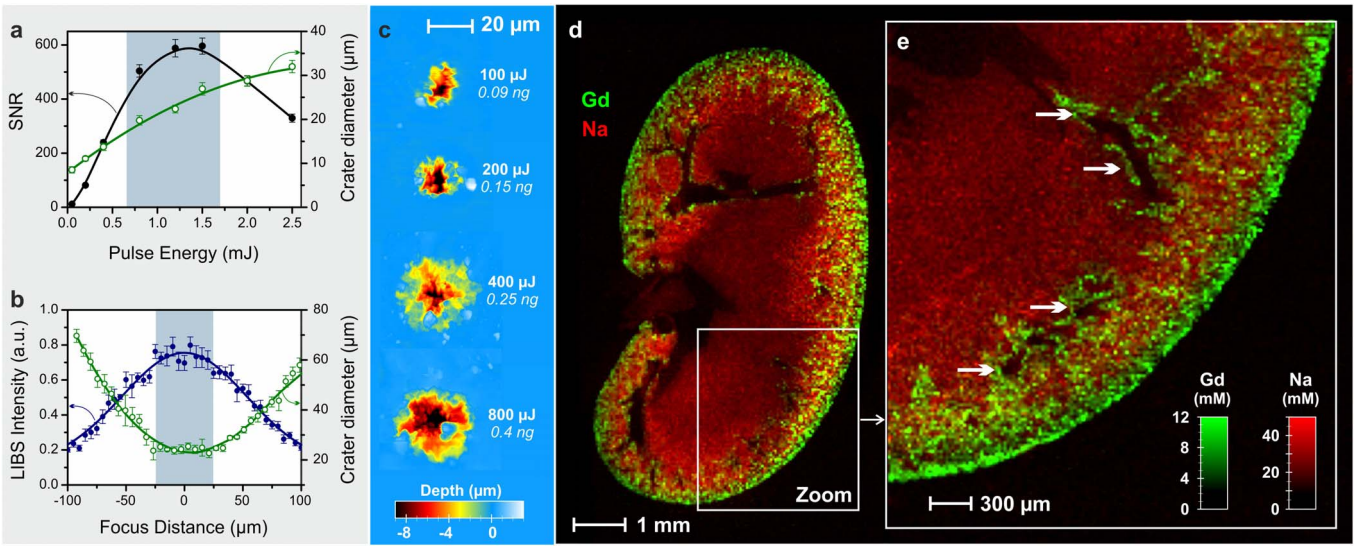

Figure 2 | Performance of LIBS microanalysis. (a), LIBS SNR for the 247.8-nm carbon line (black) measured in epoxy resin and the crater sizes measured via SEM (green) as a function of the laser pulse energy, ranging from 100 μJ to 2.5 mJ. (b), LIBS signal intensity (arbitrary units, a. u.) of the 247.8-nm carbon line (blue) and the crater sizes measured via SEM (green) as a function of the laser focus distance. A positive focus distance corresponds to a laser pulse focused below the sample surface (E = 800 μJ). (c), AFM images of craters for various pulse energies and the corresponding ablated masses. (d), Gadolinium (green) and sodium (red) biodistributions in a coronal murine kidney section, 24 hours after nanoparticle administration (spatial resolution of 40 μm). (e), Magnification of the image presented in (d) in an adjacent section with 20-μm resolution. The Gd and Na concentrations are expressed in units of millimoles per liter (mM). The white arrows indicate regions that are lacking in tissue, corresponding to blood vessels and collecting ducts.

and atomic-emission measurements are both performed using the same excitation source. The image resolution (*i.e.,* the pixel size) is limited to the size of the ablation craters, whereas the sensitivity remains strongly dependent on the amount of vaporized material and the "excitation" capability of the laser pulse. Although the use of argon combined with a sample hardener, such as epoxy resin, enables significant improvements in both these aspects compared with fresh tissue; the imaging performance must still be investigated to optimize the experimental parameters.

Therefore, we first determined the optimal laser settings with respect to the laser's pulse energy and focusing properties. Importantly, the laser pulse energy directly affects the SNR and the size of the ablation craters (Fig. 2a). As expected, the crater size increased with increasing laser energy, in contrast to the SNR, which reached a maximum for energies between 0.7 and 1.7 mJ. An excessively low energy was unable to provide sufficient excitation to the plasma, whereas an excessively high energy caused an increase in the level of continuum emission (essentially due to the radiative recombination between electrons and ions as well as Bremsstrahlung emission), representing an additional source of noise. This intermediate energy range was considered to be the nominal operating range for the LIBS microanalysis and offered both the maximum SNR (and therefore the maximum sensitivity) and resolution in the range of 20 μm. Consequently, an 800-μJ pulse energy was selected for subsequent experiments. The influence of the laser's focus position on the sample surface was also investigated for an 800-μJ pulse energy. The crater diameters and the corresponding LIBS intensities were found to be stable for laser focus positions of ±25 μm on either side of the sample surface (Fig. 2b). This fairly wide range directly resulted from the use of a low-numerical-aperture (NA) focusing objective (Fig. 1b), which allowed the entire organ to be imaged (surface area of a few tens of mm^2) using a simple sample positioning.

In addition, the morphology of the ablation craters was characterized via AFM for various pulse energies, and the amount of mass removed per pulse was also evaluated (Fig. 2c). We found that approximately 0.4 ng of matter was removed from the craters when subjected to an 800-μJ pulse energy. The calibration measurements yielded limit of detection (LoD) estimates for Gd, Si, Na, and Fe of 0.13, 0.06, 0.20, and 0.21 mM, respectively. Therefore, considering the crater volume estimated through the AFM measurements, the absolute LoD values obtained for the elements of interest were in the range of tens of attomoles per pulse. Elemental images of kidney coronal sections recorded with 40- and 20-μm resolution are presented in Fig. 2d and 2e, respectively. Both these images, which were obtained by superposing Gd (green) and Na (red) element maps, were acquired in less than one hour and represent approximately 30,000 measurements. It is worth noting that higher resolutions of 10 μm can also be obtained; however, the associated sensitivity is then altered (Supplementary Fig. 2).

Biodistribution of nanoparticles in the kidney. Figures 2d and 2e represent the bi-elemental imaging of a coronal section of a murine kidney 24 hours after intravenous (IV) administration of gadolinium-based nanoparticles. Because Na is a constitutive element of biological tissues, the Na signal was homogeneously distributed, except in regions lacking tissue, as in large collecting ducts and vessels, whereas Gd was primarily detected in the cortex region of the kidney, where the elimination process occurs, and in the outer regions of the collecting ducts (for anatomical information, see Supplementary Fig. 3). The magnified section (Fig. 2e) clearly indicated a high level of Gd in the periphery of the kidney. This region contains the Bowman's capsules, where the initial stages of blood filtration take place, as well as proximal and distal tubules.

Similarly, another kidney sample collected only 4 hours after nanoparticle administration was analyzed. As expected, this sample also reflected the accumulation of nanoparticles in the cortex and near the main collecting ducts, as indicated by the high level of Gd in this region (Fig. 3a). A high spatial correlation was observed between Gd and Si, which are the major components of the nanoparticles, with a correlation factor of $r^2 = 0.96$ (Fig. 3b). The nanoparticles contain approximately 10 Gd atoms for every 38 Si atoms (SD +/− 4 Si); thus, the theoretical molar Gd/Si ratio should be close to 1/3.8 for the native particles, as indicated by the dotted line[39]. The results indicated similar renal elimination for both elements 4 hours after

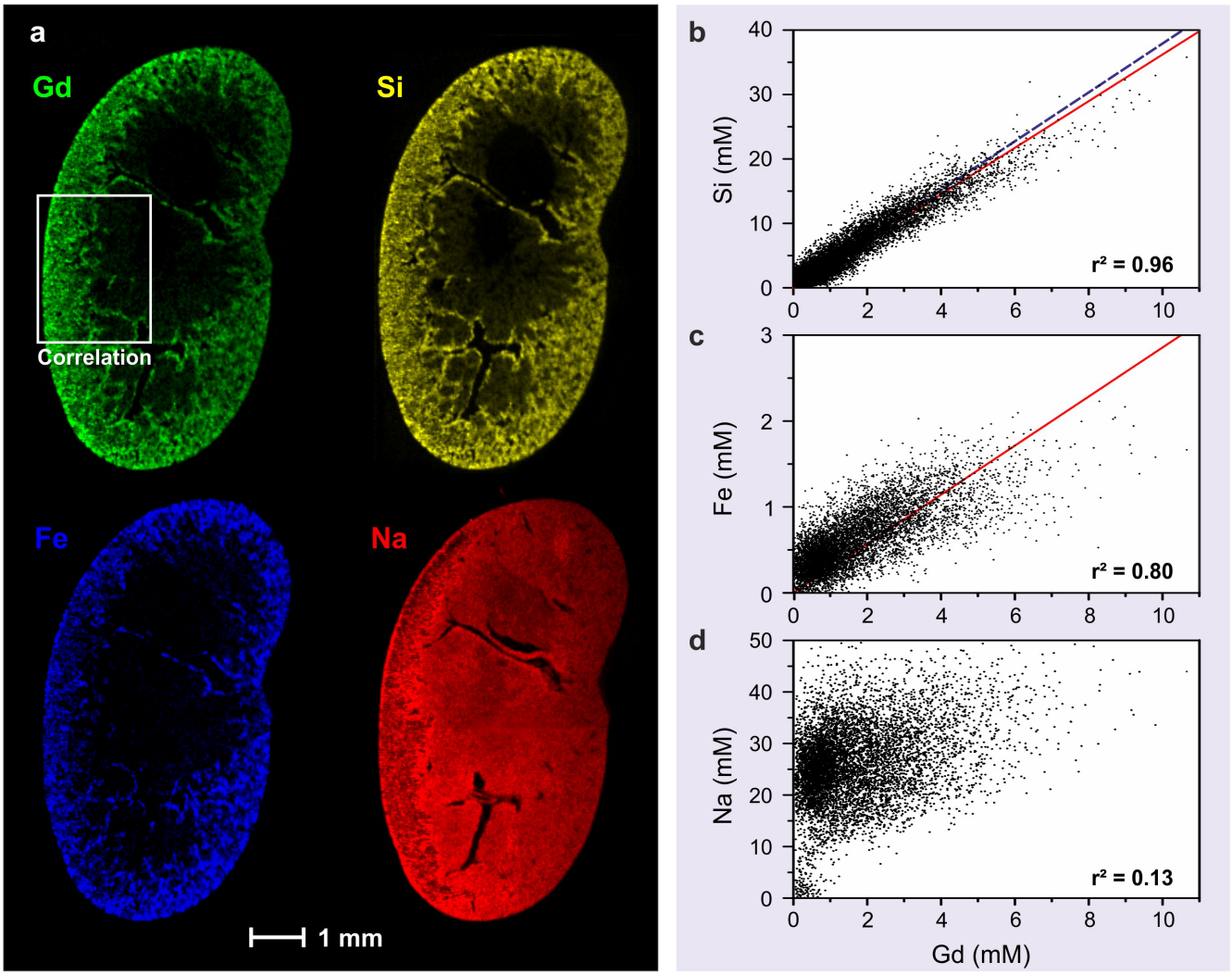

Figure 3 | Multi-elemental mapping and quantitative, spatially resolved elemental correlation. (a), Quantitative imaging of Gd, Si, Fe, and Na in a kidney coronal section, 4 hours after nanoparticle administration. The images were recorded with a 25-μm resolution and represent 60,000 pixels. (b), (c), (d), Quantitative and spatially resolved (*i.e.*, point-by-point) correlations between the concentration of Gd and the concentrations of Si (theoretical correlation represented by a dotted blue line), Fe, and Na, respectively, in the region denoted by the white rectangle in (a). The red lines represent the measured correlations.

administration of the particles. This finding suggests that 4 hours after administration, either the nanoparticles contained in the kidney were preserved before elimination or their byproducts were eliminated in a similar ratio.

A good correlation was also observed between Gd and Fe, with $r^2 = 0.80$ (Fig. 3c). The Fe signal might be correlated with the presence of blood because hemoglobin contains high levels of Fe. Physiologically, blood vessels are homogeneously distributed in the cortex region of the kidney to allow for filtration and the recycling of elements that are not eliminated in urine. A close proximity between the cells responsible for filtration (Gd signal) and the blood vessels (Fe signal) was apparent in the mapping at 25-μm resolution. As expected, the distributions of Na and Gd differed greatly, as demonstrated by the absence of any correlation between these 2 elements (Fig. 3d). This result can easily be explained by the physiological presence of Na ubiquitously within the biological tissue itself, whereas Gd was associated only with the presence of nanoparticles in precise areas of the kidney related to elimination.

To evaluate the kinetics of nanoparticle elimination, kidneys were collected at various times after nanoparticle administration (ranging from 5 min to 1 week) and were imaged for Gd and Na. The Na signal was homogeneously distributed throughout the entire kidney, independent of the time elapsed since nanoparticle injection (Fig. 4a). It was determined that the nanoparticles rapidly reached the kidneys because the Gd signal could be detected as early as 5 min after the IV injection, in good agreement with previous MRI studies[38], indicating that the nanoparticles were distributed throughout the organism and reached the kidney during the first passages of blood through this organ. As with all components filtered by the kidneys, the particles were first observed in close proximity to the cortex region, where the Bowman's capsules are located, in excellent agreement with previous nuclear imaging studies[38], before diffusing throughout the entire organ. The elimination process manifested as an increasing Gd signal that reached a maximum at 4 hours after administration, followed by a subsequent decrease. One week after injection, most of the signal had cleared, indicating effective elimination of the particles from the body via urine. The weak Gd signal observed one week after injection could be attributable to particles trapped in the proximal tubules; in this specific region of the kidney, the filtration process may retain specific components for several days before elimination[43]. These observed kinetics of elimination were in accordance with the ICP measurement performed on the entire contralateral kidney (see Fig. 4b).

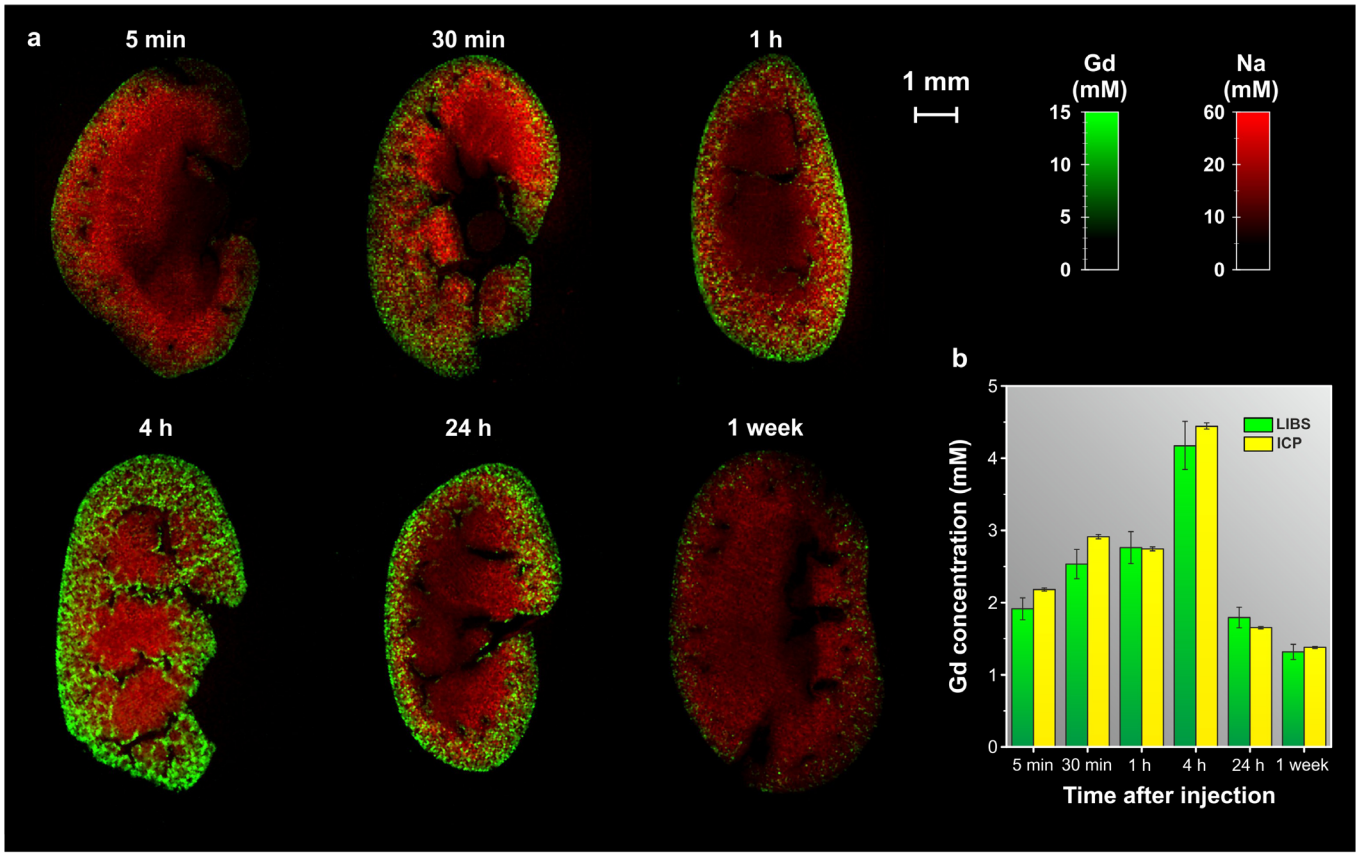

Figure 4 | Distribution of gadolinium-based nanoparticles in the kidney as a function of the time elapsed since administration. (a), Quantitative imaging of Gd and Na in kidney coronal sections. The images were recorded at a 40-µm resolution and represent 30,000 pixels. (b), Agreement between the Gd concentrations measured via LIBS (green) and ICP (yellow).

The LIBS experiments permitted imaging and quantification of the components of the nanoparticles throughout the entire kidney and provided evidence of both their rapid renal uptake and their elimination. The results highlight the appropriate elimination of nanoparticles from the organism, which is a fundamental necessity for the clinical development of such agents. Moreover, selective elimination of the byproducts may be detected based on the quantification of the 2 major elements of the nanoparticles, Gd and Si.

Discussion

We have developed a rapid all-optical, multi-elemental method for biological tissue imaging and quantification. An absolute sensitivity in the range of tens of attomoles per laser pulse was achieved for the quantification of several metallic elements, including Gd, Na, Fe, and Si. The use of epoxy-embedded samples offers better ablation control compared with fresh tissue, thus increasing the accessible resolution. Moreover, this resin enables the quantification of elements by reducing matrix effects and facilitating the preparation of calibration samples. The focusing of 266-nm UV laser pulses using a low-numerical-aperture objective allowed a 40- to 10-µm resolution to be achieved. Better resolutions can be obtained using a higher numerical aperture, which would allow investigations at the subcellular level (~µm), although with an altered sensitivity. The acquisition speed can also be improved by using higher-frequency lasers, which are commercially available. Consequently, the current combination of tissue preparation and a specific LIBS microscope configuration satisfies the requirements for the quantification of elements in most of biomedical applications, especially in terms of resolution and sensitivity. For specific application requiring higher sensitivity, the use of a second laser pulse tuned to excite specifically the element of interest would allow to improve significantly the performances in terms of sensitivity[44]. The major drawback of LIBS imaging is undeniably its invasive nature, although only a very small amount of biological material (<1 ng) is sampled during the measurement. However, material sampling based on laser ablation allows for the acquisition of depth profiles, as well as 3-dimensional images with a resolution depth of a few micrometers.

LIBS elemental analysis of biological tissue yields results that are complementary to those of conventional methods for biological investigations, such as transmission electron microscopy and immunohistochemistry, as well as to those of more complex techniques that offer higher performance under more restrictive conditions (*e.g.,* LA-ICP, nano-SIMS or µXRF). Importantly, our LIBS equipment can also be directly coupled with Raman or fluorescence imaging systems. The increasing interest in metal and organic ion distributions in biological tissues suggests that LIBS technology is likely to become a valuable investigation tool for label-free, multi-elemental imaging. This approach is highly versatile because almost any element, particularly metals, can be quantified with high sensitivity and because it can easily be used in research laboratories for routine elementary investigations in the fields of nanotechnology, biology, and medicine.

Methods

Sample preparation. These animal experiments were approved by the local ethics committee under agreement #LS-20123-004. All operative procedures related to animal are strictly conformed to the Guidelines of the French Government. Female NMRI nude mice (6–8 weeks, Janvier, Le Genest-Saint-Isle, France) were initially anesthetized with 4% isoflurane, and anesthesia was maintained with ~2% of the same gas. Gadolinium-based nanoparticles (AGuIX®, 8 µmol of Gd) were IV injected into the mice under anesthesia. Kidneys were sampled at various times from 5 minutes to 1 week after injection and were embedded in epoxy, as described elsewhere[45]. In brief, after sampling, each kidney was perfused and fixed with 2% glutaraldehyde in 0.1 M sodium cacodylate buffer (pH of 7.4) overnight at room

temperature to preserve both the tissue structure and the distribution of the particles. The samples were then rinsed three times for 10 minutes each in 0.1 M sodium cacodylate buffer and postfixed with 1% osmium tetroxide in 0.1 M sodium cacodylate buffer for 1 hour. After washing, the samples were dehydrated in a series of ethanol solutions of increasing concentration, ending with propylene oxide. The samples were then embedded in EPON (1 : 1 mixture of diglycidyl ether and dodecenylsuccinic anhydride, density of 1.22 g/L). The sample surfaces were prepared using a microtome. To allow for elemental quantification, standards containing elements of known concentrations were embedded in the same EPON resin. CH_3COONa, $(CH_3COO)_2Fe$ and AGuIX® were used as standards for Na, Fe, Gd, and Si, respectively, at 5 concentrations ranging from 1 to 40 mM. The powders were mixed with the resin (for a minimum of 4 hours), warmed for 2 days (60°C), and finally prepared using a microtome.

Experimental setup and data acquisition. The instrumental setup was based on a homemade optical microscope that combined a LIBS laser injection line, a standard optical-imaging apparatus, and a three-dimensional motorized platform for sample positioning. The LIBS experiment used quadruple Nd:YAG laser pulses of 266 nm, which were vertically focused onto the sample by a high-power 15× magnification objective (LMU-15X-266, Thorlabs) with a numerical aperture of 0.32. The pulse duration was 5 ns and the repetition rate was 10 Hz. During the experiments, the sample could be translated along 3 axes by an xyz motorized stage with a travel range of 50 mm in each direction, a maximum speed of 3 mm/s and a precision of 1 μm. The measurements were performed at room temperature and the rate of the argon gas flowing through the plasma region was set to 1.5 L/min. During the sample scan, trigonometric surface positioning was used to compensate for any flatness anomalies and to accurately control the focalization distance (the objective-to-sample distance). This system was based on the combination of a laser pointer focused obliquely onto the sample and a monitoring camera used to image the laser spot on the sample surface. A beam shutter was used to control the delivery of the laser pulse to the sample such that only one plasma plume was produced for each position in the sample. As shown in Fig. 1b, the light emitted by the plume was collected by a quartz lens (f = 2 cm) placed approximately 15 mm from the plasma plume and focused onto the entrance of an optical fiber bundle composed of 19 fibers with a 200-μm core diameter, each with a round to keyed linear arrangement. The output of the fiber bundle was connected to a Czerny-Turner spectrometer equipped with a 1200-l/mm grating blazed at 300 nm and an intensified charge-coupled device (ICCD) camera (Shamrock 303 and iStar, Andor Technology). The ICCD camera was synchronized with the Q-switch of the laser and the spectrum acquisition was performed with a delay of 300 ns and a gate of 3 μs. The width of the entrance slit of the spectrometer was set to 30 μm. In this configuration, a spectral measurement range of 30 nm was accessible with a spectral resolution of approximately 0.15 nm. To perform the mapping experiments at the greatest possible speed, the movement of the sample was synchronized with the opening of the beam shutter, and the spatial resolution was set by adjusting the speed of the translation stage. The laser energy was stabilized throughout the experiment by using a servo control loop to improve the long-term stability of the laser output. This loop was achieved by using a power meter and a computer-controlled attenuator (ATT266, Quantum Composers). Homemade software developed in the LabVIEW environment controlled the entire system and allowed for the performance of automated sequences to scan the region of interest of the tissue sample with a specific lateral resolution[42].

Construction of elemental images. An advanced spectrum treatment was developed to perform a rapid intensity extraction for each measurement site and for each species of interest. This algorithm can be applied in real time, during the mapping scan, or afterward. A single emission line was selected for each element of interest, and the algorithm defined a baseline fit using a polynomial function and subtracted it from the emission signal. Emission lines were selected based on two criteria: each selected line was required to be the strongest line in the probed range and to be unaffected by any possible interference from other lines. To retrieve the intensity signals for the elements of interest, the algorithm required less than 5 ms, suggesting that a full map (~30,000 spectra) can be processed in less than 3 minutes. A two-dimensional matrix was then provided for each species. Each cell of this matrix represented the intensity signal from a point on the sample surface for the given element and can then be displayed using a false-color scale to present a visual result in the form of elemental images. The selected emission lines and associated wavelengths are summarized in Supplementary Table I. Different spectrometer ranges could be chosen depending on the elements of interest. To measure the strongest lines associated with Gd ions in the UV-visible region, the central wavelength of the spectrometer was typically set to 333 nm. The spectral range covered in this case, from 315 to 350 nm, also allowed lines originating from Na, Ca, and Cu to be detected. In the case of Fig. 3a, which shows the spatial correlations among Si, Fe, Na, and Gd, two equivalent spectrometers were used in parallel to simultaneously detect all of the elements. All images were then processed using ImageJ software (NIH, Bethesda, MD, www.nih.gov); the images were contrasted (if necessary, and only in a linear manner), slightly smoothed (using a 0.5-pixel Gaussian smoothing), and converted from 16-bit to 8-bit images. Finally, multi-color maps were created by assigning an arbitrary color to each element (8-bit RGB images).

Quantitative measurements and limits of detection. The relative-abundance images were subsequently transformed into quantitative-abundance images after referring to the calibration measurements performed on the standard samples. Four elements were quantified: Gd, Si, Na, and Fe. Calibration measurements for the elements of interest were performed prior to each mapping analysis by recording a sequence of 50 × 50 spectra for each standard. Linear regressions were then obtained by applying the least-squares method to the experimental data. The limit of detection (LoD) values were estimated as 3 times the background noise divided by the slope of the analytical curve. The LoD values determined for the 4 elements in the nominal operating range (energy per pulse of 800 μJ) are presented in Supplementary Table 1 and are expressed in units of both mM and weight ppm. The relative measurement accuracy was estimated between 6 to 8% depending on elements from obtained linear regressions.

Complementary techniques. Ablation craters were observed under various experimental conditions via scanning electron microscopy (SEM) and atomic force microscopy (AFM). SEM observations were performed using an ESEM XL30-FEI microscope equipped with a thermal field emission gun (FEG). SEM images were used to estimate the crater diameters obtained in epoxy resin as a function of laser energy and focus distance (*i.e.,* figure 2a and 2b). AFM experiments were performed using an Asylum MFP 3D operating in tapping mode. The z-axis scan sensor could travel up to 15 μm, allowing for the measurement of large samples. For all images, the scan field was 70 × 70 μm^2, whereas the scan rate was 0.45 Hz, to ensure good regulation of the feedback loop. Crater volumes were determined for various laser energies (*i.e.,* figure 2c) by performing an integration of AFM images in depth.

The concentration of gadolinium in the kidney samples was determined via ICP-MS (inductively coupled plasma-mass spectrometry) using a Varian® 710-ES spectrometer. The samples were dispersed in 5 mL of aqua regia (67% HNO_3/37% hydrochloric acid (w/w)) for 4 hours at 80°C. Subsequently, the samples were diluted with HNO_3 5% (w/w) matrix to adjust the volume to 10 mL; the samples were then filtered (0.22 μm) and analyzed. For calibration of the ICP-MS, single-element standard solutions were used and prepared from a 1000-ppm Gd standard acquired from SCP Science® by successive dilutions with a HNO_3 5% (w/w) matrix. Importantly, in each experiment, the right kidney of each animal was sectioned for LIBS analysis, and the left kidney of the same animal was used for ICP measurement.

1. Garini, Y., Vermolen, B. J. & Young, I. T. From micro to nano: recent advances in high-resolution microscopy. *Curr. Opin. Biotechnol.* **16**, 3–12 (2005).
2. Hao, X. *et al.* From microscopy to nanoscopy via visible light. *Light. Sci. Appl.* **2**, 108 (2013).
3. Mahou, P. *et al.* Multicolor two-photon tissue imaging by wavelength mixing. *Nat. Methods* **9**, 815–818 (2012).
4. Si, K., Fiolka, R. & Cui, M. Fluorescence imaging beyond the ballistic regime by ultrasound pulse guided digital phase conjugation. *Nat. Photonics* **6**, 657–661 (2012).
5. Flusberg, B. A. *et al.* Fiber-optic fluorescence imaging. *Nat. Methods* **2**, 941–950 (2005).
6. Qian, X. *et al.* In vivo tumor targeting and spectroscopic detection with surface-enhanced Raman nanoparticle tags. *Nat. Biotechnol.* **26**, 83–90 (2008).
7. Razansky, D. *et al.* Multispectral opto-acoustic tomography of deep-seated fluorescent proteins in vivo. *Nat. Photonics* **3**, 412–417 (2009).
8. Wang, L. V. & Hu, S. Photoacoustic tomography: in vivo imaging from organelles to organs. *Science* **335**, 1458–1462 (2012).
9. Freudiger, C. W. *et al.* Label-free biomedical imaging with high sensitivity by stimulated Raman scattering microscopy. *Science* **322**, 1857–1861 (2008).
10. Freudiger, C. W. *et al.* Stimulated Raman scattering microscopy with a robust fibre laser source. *Nat. Photonics* **8**, 153–159 (2014).
11. Itoh, K. & Ozeki, Y. Raman spectroscopy: Molecular discrimination imaging. *Nat. Photonics* **5**, 71–72 (2011).
12. Saar, B. G. *et al.* Video-rate molecular imaging in vivo with stimulated Raman scattering. *Science* **330**, 1368–1370 (2010).
13. Chao, W., Harteneck, B. D., Liddle, J. A., Anderson, E. H. & Attwood, D. T. Soft X-ray microscopy at a spatial resolution better than 15 nm. *Nature* **435**, 1210–1213 (2005).
14. Pascolo, L. *et al.* The interaction of asbestos and iron in lung tissue revealed by synchrotron-based scanning X-ray microscopy. *Sci. Rep.* **3**, 1123 (2013).
15. Wogelius, R. A. *et al.* Trace metals as biomarkers for eumelanin pigment in the fossil record. *Science* **333**, 1622–1626 (2011).
16. Sakdinawat, A. & Attwood, D. T. Nanoscale X-ray imaging. *Nat. Photonics* **4**, 840–848 (2010).
17. Kraft, M. L. & Klitzing, H. A. Imaging lipids with secondary ion mass spectrometry. *Biochim. Biophys. Acta.* **1841**, 1108–1119 (2014).
18. Austin, C. *et al.* Barium distributions in teeth reveal early-life dietary transitions in primates. *Nature* **498**, 216–219 (2013).
19. Shariatgorji, M., Svenningsson, P. & Andren, P. E. Mass spectrometry imaging, an emerging technology in neuropsychopharmacology. *Neuropsychopharmacology* **39**, 34–49 (2014).
20. Watrous, J. D. & Dorrestein, P. C. Imaging mass spectrometry in microbiology. *Nat. Rev. Microbiol.* **9**, 683–694 (2011).
21. Zoriy, M., Dehnhardt, M., Matusch, A. & Becker, J. S. Comparative imaging of P, S, Fe, Cu, Zn and C in thin section of rat brain tumor as well as control tissues by laser ablation inductively couples plasma mass spectrometry. *Spectrochim. Acta B.* **63**, 375–382 (2008).

22. Lei, P. *et al*. Tau deficiency induces parkinsonism with dementia by impairing APP-mediated iron export. *Nat. Med.* **18**, 291–295 (2012).
23. Cremers, D. A. & Radziemski, L. J. *Handbook of Laser-Induced Breakdown Spectroscopy.* (Wiley, Chichester, 2006).
24. Miziolek, A. W., Palleschi, V. & Schechter, I. *Laser-Induced Breakdown Spectroscopy: Fundamentals and Applications.* (Cambridge University Press, 2006).
25. Harmon, R. S., Russo, R. E. & Hark, R. R. Applications of laser-induced breakdown spectroscopy for geochemical and environmental analysis: A comprehensive review. *Spectrochim. Acta B.* **87**, 11–26 (2013).
26. Dixon, P. B. & Hahn, D. W. Feasibility of Detection and Identification of Individual Bioaerosols Using Laser-Induced Breakdown Spectroscopy. *Anal. Chem.* **77**, 631–638 (2005).
27. Meslin, P. Y. *et al*. Soil diversity and hydration as observed by ChemCam at Gale crater, Mars. *Science* **341**, 1238670 (2013).
28. Williams, R. M. *et al*. Martian fluvial conglomerates at Gale crater. *Science* **340**, 1068–1072 (2013).
29. Bette, H. & Noll, R. High-speed laser-induced breakdown spectrometry for scanning microanalysis. *J. Phys. D.* **37**, 1281–1288 (2004).
30. Ma, Q. *et al*. Multi-elemental mapping of a speleothem using laser-induced breakdown spectroscopy. *Spectrochim. Acta B.* **65**, 707–714 (2010).
31. Menut, D., Fichet, P., Lacours, J.-L., Rivoallan, A. & Mauchien, P. Micro-laser-induced breakdown spectroscopy technique: a powerful method for performing quantitative surface mapping on conductive and nonconductive samples. *Appl. Opt.* **42**, 6063–6071 (2003).
32. Motto-Ros, V. *et al*. Mapping of native inorganic elements and injected nanoparticles in a biological organ with laser-induced plasma. *Appl. Phys. Lett.* **101**, 223702 (2012).
33. Motto-Ros, V. *et al*. Mapping nanoparticles injected into a biological tissue using laser-induced breakdown. *Spectrochim. Acta B.* **87**, 168–174 (2013).
34. Paul, A. *et al*. A nanobiohybrid complex of recombinant baculovirus and Tat/DNA nanoparticles for delivery of Ang-1 transgene in myocardial infarction therapy. *Biomaterials* **32**, 8304–8318 (2011).
35. Sahoo, S. K., Parveen, S. & Panda, J. J. The present and future of nanotechnology in human health care. *Nanomedicine* **3**, 20–31 (2007).
36. Wagner, V., Dullaart, A., Bock, A. K. & Zweck, A. The emerging nanomedicine landscape. *Nat. Biotechnol.* **24**, 1211–1217 (2006).
37. Wang, A. Z., Langer, R. & Farokhzad, O. C. Nanoparticle delivery of cancer drugs. *Annu. Rev. Med.* **63**, 185–198 (2012).
38. Lux, F. *et al*. Ultrasmall rigid particles as multimodal probes for medical applications. *Angew. Chem. Int. Ed. Engl.* **50**, 12299–12303 (2011).
39. Mignot, A. *et al*. A top-down synthesis route to ultrasmall multifunctional gd-based silica nanoparticles for theranostic applications. *Chemistry* **19**, 6122–6136 (2013).
40. Zhai, X. Y., Kristoffersen, I. B. & Christensen, E. I. Immunocytochemistry of renal membrane proteins on epoxy sections. *Kidney Int.* **72**, 731–735 (2007).
41. Glauert, A. M., Glauert, R. H. & Rogers, G. E. A new embedding medium for electron microscopy. *Nature* **178**, 803 (1956).
42. Motto-Ros, V., Negre, E., Pelascini, F., Panczer, G. & Yu, J. Precise alignment of the collection fiber assisted by real-time plasma imaging in laser-induced breakdown spectroscopy. *Spectrochim. Acta B.* **92**, 60–69 (2014).
43. Abdelhalim, M. A. & Abdelmottaleb Moussa, S. A. The gold nanoparticle size and exposure duration effect on the liver and kidney function of rats: In vivo. *Saudi. J. Biol. Sci.* **20**, 177–181 (2013).
44. Laville, S. *et al*. Laser-induced fluorescence detection of lead atoms in a laser-induced plasma: An experimental analytical optimization study. *Spectrochim. Acta B.* **64**, 347–353 (2009).
45. Rima, W. *et al*. Internalization pathways into cancer cells of gadolinium-based radiosensitizing nanoparticles. *Biomaterials* **34**, 181–195 (2013).

Acknowledgments

The authors gratefully acknowledge the LABEX iMUST (ANR-10-LABX-0064) and PRIMES (ANR-11-LABX-0063) of Lyon 1 University within the programs "Investissements d'Avenir" (ANR-11-IDEX-0007 and ANR-11-IDEX-0007, respectively), operated by the French National Research Agency (ANR) within the project EMILI, as well as the Lyon Science Transfert, for financial support. We also heartily acknowledge the CTμ (A. Rivoire and C. Boule) and F. Pelascini (CRITT Matériaux Alsace) for fruitful discussions and advice regarding epoxy samples and standards.

Author contributions

L.S. and V.M. contributed equally to this work. L.S. prepared all the biological samples. V.M. developed the LIBS system and data software. L.S. and V.M. prepared all figures shown in the manuscript. G.P. and J.Y. contributed to designing the LIBS experiment. L.S., V.M., B.B. and S.K. analyzed the samples, treated the data, and wrote the main manuscript text. J.-M.B. and A.P. performed the AFM investigations, and participated in writing the article. F.L. and O.T. participated in writing the article. All authors reviewed the manuscript.

Additional information

Supplementary information accompanies this paper at http://www.nature.com/scientificreports

Competing financial interests: We declare that the authors have no competing interests as defined by Nature Publishing Group, or other interests that might be perceived to influence the results and discussion reported in this paper.

How to cite this article: Sancey, L. *et al*. Laser spectrometry for multi-elemental imaging of biological tissues. *Sci. Rep.* **4**, 6065; DOI:10.1038/srep06065 (2014).